Title

Direct observation of ring-opening dynamics in strong-field ionized selenophene using femtosecond inner-shell absorption spectroscopy

Journal

The Journal of Chemical Physics, 145(23)

ISSN

0021-9606

Authors

Lackner, Florian

Chatterley, Adam S

Pemmaraju, CD

et al.

Publication Date

2016-12-21

DOI

10.1063/1.4972258

Peer reviewed

Direct observation of ring-opening dynamics in strong-field ionized selenophene using femtosecond inner-shell absorption spectroscopy

Florian Lackner, Adam S. Chatterley, C. D. Pemmaraju, Kristina D. Closser, David Prendergast, Daniel M. Neumark, Stephen R. Leone, and Oliver Gessner

Citation: J. Chem. Phys. **145**, 234313 (2016); doi: 10.1063/1.4972258
View online: http://dx.doi.org/10.1063/1.4972258
View Table of Contents: http://aip.scitation.org/toc/jcp/145/23
Published by the American Institute of Physics

Direct observation of ring-opening dynamics in strong-field ionized selenophene using femtosecond inner-shell absorption spectroscopy

Florian Lackner,[1,2] Adam S. Chatterley,[1,2] C. D. Pemmaraju,[1,3] Kristina D. Closser,[3] David Prendergast,[3] Daniel M. Neumark,[1,2] Stephen R. Leone,[1,2,4] and Oliver Gessner[1]
[1]*Chemical Sciences Division, Lawrence Berkeley National Laboratory, Berkeley, California 94720, USA*
[2]*Department of Chemistry, University of California, Berkeley, California 94720, USA*
[3]*The Molecular Foundry, Lawrence Berkeley National Laboratory, Berkeley, California 94720, USA*
[4]*Department of Physics, University of California, Berkeley, California 94720, USA*

(Received 10 June 2016; accepted 2 December 2016; published online 21 December 2016)

Femtosecond extreme ultraviolet transient absorption spectroscopy is used to explore strong-field ionization induced dynamics in selenophene (C_4H_4Se). The dynamics are monitored in real-time from the viewpoint of the Se atom by recording the temporal evolution of element-specific spectral features near the Se 3d inner-shell absorption edge (~58 eV). The interpretation of the experimental results is supported by first-principles time-dependent density functional theory calculations. The experiments simultaneously capture the instantaneous population of stable molecular ions, the emergence and decay of excited cation states, and the appearance of atomic fragments. The experiments reveal, in particular, insight into the strong-field induced ring-opening dynamics in the selenophene cation, which are traced by the emergence of non-cyclic molecules as well as the liberation of Se^+ ions within an overall time scale of approximately 170 fs. We propose that both products may be associated with dynamics on the same electronic surfaces but with different degrees of vibrational excitation. The time-dependent inner-shell absorption features provide direct evidence for a complex relaxation mechanism that may be approximated by a two-step model, whereby the initially prepared, excited cyclic cation decays within $\tau_1 = 80 \pm 30$ fs into a transient molecular species, which then gives rise to the emergence of bare Se^+ and ring-open cations within an additional $\tau_2 = 80 \pm 30$ fs. The combined experimental and theoretical results suggest a close relationship between σ* excited cation states and the observed ring-opening reactions. The findings demonstrate that the combination of femtosecond time-resolved core-level spectroscopy with *ab initio* estimates of spectroscopic signatures provide new insights into complex, ultrafast photochemical reactions such as ring-opening dynamics in organic molecules in real-time and with simultaneous sensitivity for electronic and structural rearrangements. *Published by AIP Publishing.* [http://dx.doi.org/10.1063/1.4972258]

I. INTRODUCTION

Among photo-induced molecular dynamics, ring-opening reactions are attracting particular attention due to their fundamental importance for organic chemistry, including chemical synthesis and biological function.[1] While key aspects of the molecular orbitals underlying ring-opening were developed by Woodward and Hoffman in 1969,[2] recent advances in ultrafast laser spectroscopy and diffractive imaging now enable the study of this class of reactions in real-time.[3,4] Here, we present a novel approach, femtosecond extreme ultraviolet (XUV) transient absorption spectroscopy to explore a photo-induced ring-opening reaction in the selenophene cation ($C_4H_4Se^+$) from the unique perspective of the selenium atom and with a temporal resolution commensurate with some of the fundamental dynamic time scales.

The molecular structure and electronic spectra of selenophene have been studied previously both theoretically[5,6] and experimentally.[5,7] Selenophene[8] and its heterocyclic five-membered analogues, such as furan[9] and thiophene,[10–13] can undergo an electrocyclic reaction upon photoexcitation during which the aromatic ring is opened. In particular for thiophene and selenophene, a deeper understanding of these ring-opening processes is sought to better understand their strengths and weaknesses with respect to applications in organic electronics.[14,15]

Strong-field ionization (SFI) of polyatomic molecules leads to complex dynamics that may involve multiple ionic continua and dissociation channels.[16–18] Deciphering the underlying physical mechanisms remains challenging for both experimental and theoretical studies. XUV transient absorption (TA) spectroscopy has previously been employed to study strong-field induced dynamics in molecules such as C_2H_3Br,[19] CH_2Br_2,[20] or Br_2[21] and, very recently, in 1,2-dibromoethane.[22] The method explores fundamental electronic and nuclear dynamics by recording the time-dependent absorption spectrum associated with the excitation of element-specific core-level electrons. It provides access to ultrafast time scales reaching the attosecond regime[23] and may be used to monitor intense-field-induced effects such as light-induced transparency and electronic alignment.[24–27] XUV TA has been applied to explore strong-field[19,21,24] and single UV photon-induced[28,29] molecular dynamics from the unique perspective of distinct reporter atoms.[30]

Here, SFI induced dynamics in selenophene (C_4H_4Se) are explored by femtosecond transient XUV absorption spectroscopy at the Se 3d edge (~58 eV).[31] The interpretation of the observed time-dependent core-level absorption spectra is supported by first-principles time-dependent density functional theory (TDDFT) based simulations of XUV absorption spectra for a series of benchmark molecular configurations. Along with the instantaneous creation of stable parent cations, transient spectral signatures of selenophene ions in a variety of excited states are observed as well as the appearance of atomic fragments. In particular, non-cyclic cations, most likely in σ^* excited states, are formed on an overall time scale of 170 fs. Additionally, a significant fraction of the selenophene ions undergoes a ring-opening process on the same time scale in which both C–Se bonds are eventually broken to produce isolated Se^+ ions. The dynamics leading to both ring-opening products may be approximated by a two-step model, whereby an initially prepared cyclic cation decays within $\tau_1 \approx 80$ fs into a transient molecular species, which further decays within an additional $\tau_2 \approx 80$ fs to form the two different products. It is speculated that both the dissociative and the non-dissociative product channels may be associated with dynamics that proceed on the same electronic surfaces but with different degrees of vibrational excitation. The study demonstrates that the combination of ultrafast XUV transient absorption spectroscopy with state-of-the-art first principle calculations may be used to gain a deeper insight into complex photochemical processes by monitoring electronic and structural dynamics in real-time and from the perspective of well-defined reporter atoms. In particular, the simultaneous sensitivity of transient inner-shell spectroscopy to both neutral and ionic intermediates and products enables a detailed analysis of the large manifold of dynamic pathways that is often accessed by SFI.

II. EXPERIMENTAL

A detailed description of the experimental setup has been given elsewhere.[19,27] In brief, the output of a femtosecond Ti:sapphire laser (780 nm center wavelength, ~3.3 mJ pulse energy at 3 kHz, 40 fs pulse width (full-width-at-half-maximum, FWHM)) is split 50:50 into a beam of NIR "pump" pulses and a beam that drives a high-order harmonic generation (HHG) source to produce femtosecond XUV "probe" pulses. The pump beam is routed through a computer-controlled delay stage to vary the time delay between the pump- and probe-pulses. The HHG driving beam is focused into a semi-infinite HHG gas cell, filled with about 75 Torr of neon. Under these conditions, HHs covering the spectral range from 45 eV to the Al L-edge at 72 eV are generated. XUV light beyond 72 eV is suppressed by Al filters used to block the NIR driving laser and IR stray light from the pump laser. A toroidal mirror is used to focus the XUV probe beam into a ceramic sample cell, where it is spatially overlapped with the NIR pump beam. The cell is connected to a reservoir filled with liquid selenophene and separately a xenon gas bottle outside the chamber. Both beams enter and exit the sample cell through 750 μm wide orifices. The focus diameters ($1/e^2$) of the XUV and NIR beams are determined to be (23 ± 5) μm and (85 ± 15) μm, respectively, by knife-edge scans (XUV) and using a beam profiler (NIR). The larger diameter of the IR pump beam compared to the XUV probe beam and Rayleigh ranges of the beams far beyond the interaction region ensure a nearly uniform electrical field in the overlap region inside the sample cell. The pump pulse intensity, ranging from 0.7 to 3×10^{14} W/cm^2, is estimated using a power meter and the measured pump beam diameter. The intensity calibration is confirmed by measuring the NIR power-dependent Xe^+/Xe^{++} signal ratio, which typically agrees with literature values to within a factor of 2 or better.[22] Note that this uncertainty only applies to the absolute NIR intensity. Errors in relative intensities when comparing different measurements are estimated to be <10%, including the reproducibility of the pump-probe overlap.

Strong-field induced changes in the XUV absorption spectrum of xenon are used to calibrate the XUV energy axis and t_0, i.e., the delay stage position for zero pump-probe delay.[27] The instrument response function (IRF) of 67 ± 12 fs is derived from the pump-probe time trace of the molecular HOMO-1 hole signal that appears instantaneously within the time resolution of the experiment. Note that the IRF derived from Xe calibration experiments is about 40 fs. However, the selenophene data have been acquired over several days (in contrast to our recent work on DBE),[22] including many sample cell cleaning cycles. Rapidly alternating runs using Xe and selenophene are currently not possible due to different sample cell requirements. The specified 67 fs IRF thus accounts for any long-term variations in the system affecting t_0 as well as the pump- and probe-pulse widths. In contrast to this unavoidable slight temporal broadening, corresponding variations in the pump pulse intensity and the crucial spatial pump-probe overlap are constantly monitored and corrected for. This is achieved by keeping the pump-probe signal intensity and, in particular, the ratio between emerging Se^+ fragment signals and parent molecule depletion signals constant. Both observables vary strongly with the pump intensity within the probed sample volume and are thus sensitive probes of both the NIR intensity and the spatial pump-probe overlap.

A mechanical chopper that blocks the pump beam at a frequency of 4 Hz is used to record "pump-on" and "pump-off" spectra almost simultaneously, which significantly reduces the impact of high-harmonics intensity fluctuations on the pump-probe traces. For each pump-probe delay, 34 runs are averaged with integrated exposure times of 10 s under pump-on and 10 s under pump-off conditions.

After passing the sample cell, the XUV light is dispersed by a concave variable-line-spacing grating and detected by an X-ray CCD camera. The spectrometer is calibrated before each series of selenophene experiments. The uncertainty of the energy calibration is <60 meV, which is used as the lower limit for peak position uncertainties obtained from any fitting procedures. The absolute energy resolution of the spectrometer has been determined to be ~100 meV over the entire spectral range of interest from the recorded Xe spectra. Note that the uncertainty of the energy calibration is smaller than the absolute energy resolution of the spectrometer due to the fact that the uncertainty of a peak's centroid position is usually smaller than the peak width.

The optical density of the sample is determined by $OD = \log(I_{ref}/I_{sig})$, where I_{sig} and I_{ref} are the detected XUV

signal intensities with and without sample molecules, respectively, in the gas cell. Positive time delays indicate that the NIR pump pulse arrives at the sample before the XUV probe pulse. The pump pulse induced changes in optical density are described by $\Delta OD = \log(I_{pump\text{-}off}/I_{pump\text{-}on})$, whereby the pump laser passes through the mechanical chopper when $I_{pump\text{-}on}$ is recorded and the beam is blocked to record $I_{pump\text{-}off}$. Note that the static determination of the sample OD and the time-dependent measurements of NIR-induced optical density changes ΔOD are performed at different cell pressures since both experiments require a different compromise between signal strengths and cell cleaning cycles. The absolute values for OD and ΔOD are, therefore, not directly comparable.

In the data analysis a filter procedure is applied that excludes spectra with excessive ΔOD variations originating from instabilities of the HHG source that are not mediated by the chopper technique. The excluded spectra contain artifacts that are similar in size to the spectral features themselves. Outliers are identified separately for each experimental run by analyzing the root-mean-square (RMS) values of the ΔOD scatter in the nominally featureless spectral region beyond 63 eV. Large artifacts in this region lead to correspondingly high RMS values. Typically, spectra are excluded from further analysis if their ΔOD RMS values differ by more than two FWHM of the RMS distribution from its mean. This ensures that no significant information is lost while clear artifacts in the spectra are avoided.

The uncertainty ranges of all presented spectra are estimated by dividing the standard deviation of up to 34 separate acquisition runs per data point by the square root of the number of runs (after removing the outliers). Note that some residual variations in experimental parameters such as the high-order harmonics flux or the sample cell pressure contribute systematic errors that affect many or all data points in a spectrum in a correlated fashion. The given uncertainty ranges include these additional error sources, which is why they appear relatively large compared to the scatter of the data points.

III. THEORETICAL METHODS

Interpretation of the experimentally observed transient XUV spectral features is aided by first principles simulations of XUV absorption spectra in strong field ionized selenophene. To this end the Se $M_{IV\text{-}V}$ edge XUV spectral fingerprints of a series of neutral, charged, and electronically excited configurations of selenophene are computed. A comparison of these to experimental spectra enables the assignment of the character of some of the observed transient features (see discussion in the supplementary material). The theoretical simulations are based on a combination of density functional theory (DFT)[32,33] and time-dependent density functional theory (TDDFT)[34] methods for estimating excited-state properties and consist of a two-step procedure for calculating transient XUV spectra: in the first step, optimized geometries for the ground states and several low-energy valence excited-states of C_4H_4Se and $C_4H_4Se^+$ are computed using the maximum overlap method (MOM).[35] Thus, the minimum point on the potential energy surface of each low-energy excited configuration is considered through the MOM approach. The second step then involves calculating the Se $M_{IV\text{-}V}$ edge absorption spectrum for each such configuration using a restricted energy window (REW)[36] linear-response TDDFT[37] formalism. All simulations employ an asymptotically correct range-separated hybrid exchange-correlation functional based on the ωPBE[38] class of functionals. In particular, for the TDDFT XUV absorption calculations that require a simultaneous description of both core and valence electronic states, we tune the range separation parameters within the hybrid functional to enforce the Koopmans' condition,[39] whereby the DFT eigenvalue of a given occupied eigenstate is brought into agreement with the corresponding electron removal energy for that state, on both the Se 3d and HOMO states simultaneously (see supplementary material for details). We find that this procedure yields good agreement between experimental and theoretical line shapes for the Se $M_{IV\text{-}V}$ edge XUV spectrum of ground state C_4H_4Se. The same tuned functional is then used to calculate spectra for all the other configurations considered. Additional details on basis sets and other simulation parameters are provided in the Computational Details subsection of section S1 in the supplementary material. Throughout the manuscript, the theoretically derived spectra are convoluted with a Gaussian of 0.47 eV FWHM to account for lifetime broadening and the instrumental energy resolution to facilitate an easier comparison between theory and experiment.

IV. RESULTS

A. Static XUV absorption spectrum

Figure 1(a) shows the measured static XUV absorption spectrum of selenophene (red, recorded without a pump laser beam) along with the result of a fit procedure (blue) that models the spectrum by a set of six Gaussian peaks. The sloped background that decreases with increasing photon energy has been included as a quadratic baseline for each Gaussian peak. The measured spectrum exhibits four readily recognizable peaks a-d. The features originate from transitions of $3d_{5/2}$ and $3d_{3/2}$ core-level electrons into empty valence (LUMO and LUMO+1) and Rydberg orbitals. In particular, the main peaks a, b comprise overlapping $\sigma^* \leftarrow 3d_{5/2,3/2}$ and $\pi^* \leftarrow 3d_{5/2,3/2}$ transitions.[40] The energy splitting within each set of double peaks ((0.77 ± 0.08) eV for peaks a, b and (0.76 ± 0.08) eV for peaks c, d) resembles the spin-orbit (SO) splitting of the 3d core-levels in atomic selenophene (0.9 eV).[31] Note, however, that the ratio of the peak intensities a and b does not reflect the branching ratio of 3/2 that would be expected from spin-statistics if a and b would be associated purely with transitions involving $3d_{5/2}$ and $3d_{3/2}$ orbitals, respectively. Instead, both peaks comprise contributions from both orbitals, which are estimated in the fit by four Gaussian peaks with variable widths, heights, and positions but fixed peak pair spacing (0.9 eV) and ratios (3/2). The fit result is illustrated in Figure 1(a) by two solid and two dashed curves for transitions into σ* and π* orbitals, respectively. Features c and d are modeled by two additional Gaussian peaks (green) with center energies of 59.82 ± 0.06 eV and 60.57 ± 0.06 eV, respectively, which are assigned to core level transitions into Rydberg orbitals. We emphasize that the multi-parameter fit describing features a and b is not entirely free running and is not meant

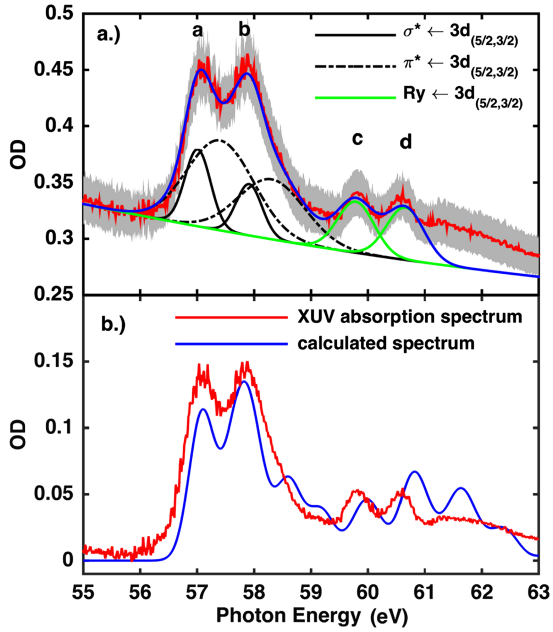

FIG. 1. (a) Experimental XUV absorption spectrum (red) with grey shaded 1σ uncertainty range. The two peaks a, b at (57.08 ± 0.06) eV and (57.85 ± 0.06) eV are described by a superposition of four Gaussian peaks (blue curve) corresponding to transitions from Se $3d_{5/2}$ and $3d_{3/2}$ core levels into unoccupied σ* and π* valance orbitals (black solid and dashed curves, respectively). Features c and d are assigned to core-level to Rydberg-orbital transitions (green curves). Spectral assignments are based on the results of a DFT based *ab initio* simulation of the XUV absorption spectrum shown as a blue curve in (b) in comparison to the experimental data in red. The experimental spectrum in (b) has been corrected for the sloped background from valence ionization since theory only accounts for the Se 3d core-level transitions.

to provide a unique spectral assignment but rather a demonstration that a weighted combination of a SO split set of σ* and π* transitions, as suggested by Hitchcock *et al.*,[40] and our calculations can be used to provide a good description of the measured spectrum.

The assignment of the fit model functions to specific transitions is based on a comparison of the measured XUV absorption spectrum with a DFT based simulation as illustrated in Figure 1(b). Note that the experimental spectrum (red) has been corrected for the broad background originating from non-resonant valence-shell ionization,[28,40] which is not considered in the calculation (blue). The main features a, b are well described by theory, which also approximately reproduces the positions of the isolated Rydberg transitions. However, theory overestimates the intensity and slightly offsets the spectral position of transitions beyond 60 eV. The width of the $\pi^* \leftarrow 3d_{5/2,3/2}$ transitions is overestimated by the fit (Figure 1(a)) because it does not account for spectral features between the σ* and π* transitions and the Rydberg features, which can be seen in the calculated spectrum around 59 eV. We note that our assignment of the 3d core-level transitions into σ* and π* orbitals is reversed compared to the one proposed by Hitchcock and co-workers.[40] The results of our DFT calculation predict that the lowest energy transition from the deep-lying 3d orbitals into the σ* orbital is lower in energy than the corresponding one into the π* orbital despite the fact that the π* orbital is the LUMO and the σ* orbital the LUMO+1 orbital within the molecule's neutral ground state configuration, as described in the supplementary material. A similar effect has previously been observed in guanidinium[41] and might represent a general phenomenon for small molecule core-level excitations with significant differences in localization of σ* and π* orbitals about the core-excited atom.

B. Transient absorption spectra

Figure 2 shows a waterfall representation of the XUV transient absorption spectra recorded with pump-probe delays between −250 and 750 fs and spanning photon energies from 52 to 62 eV, where the $t = 0$ spectrum is highlighted in red. The data were acquired using a pump pulse intensity of 3×10^{14} W/cm^2. Three different types of time-dependent signals are observed: (i) regions exhibiting negative ΔOD (dark blue) after $t = 0$, (ii) several transient features visible around $t = 0$, most prominent at about 56 eV and 59 eV (positive ΔOD, peak B and C), and (iii) a set of sharp features around 54 eV (positive ΔOD, red) that exhibit an apparent delayed onset relative to time zero and then remain constant within the range of the experiment.

In order to determine the different spectral contributions and their dynamics in more detail, we compare spectra recorded within two different pump-probe delay ranges that emphasize different spectral features. Figure 3 compares the average spectrum associated with delays between 0 fs and 40 fs (blue) with the average spectrum related to delays between 280 fs and 2000 fs (red). The sharp spectral lines between 52 and 55 eV are assigned to fragment Se^+ ions based on a comparison to the previously determined XUV absorption spectrum of isolated Se^+ ions[42] (black curve in Figure 3, this spectrum has been shifted by −0.08 eV to match the recorded spectrum). The prominent, instantly appearing negative ΔOD features at 57 eV and 58 eV as well as near 60 eV and 61 eV

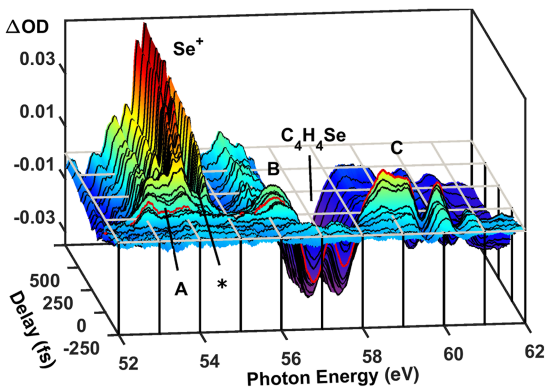

FIG. 2. Waterfall representation of transient XUV absorption spectra recorded at a pump pulse intensity of 3×10^{14} W/cm^2. The $t = 0$ spectrum is plotted in red. Depletion of neutral selenophene molecules (C_4H_4Se) appears instantaneously, as indicated by the drop of the features near 57.5 eV (compare to Figure 1). The sharp, very intense features between 53 and 55 eV correspond to emerging bare Se^+ ions. A broad molecular feature A is visible immediately after $t = 0$, whereas the much stronger Se^+ signals emerge with an apparent delay. Transient molecular features B and C appear around 56 and 59 eV, respectively. While feature C is only visible near $t = 0$, feature B decays initially, then remains constant at longer times and expands spectrally toward lower energies.

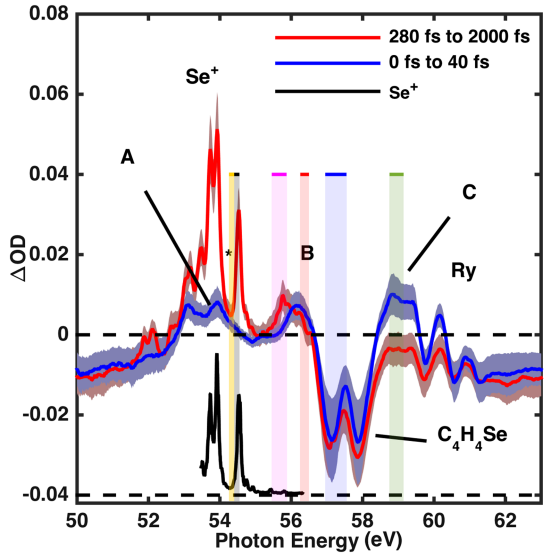

FIG. 3. Comparison of the long-time delay spectrum (red, averaged over pump-probe delays 280-2000 fs) and the spectrum near t_0 (blue, averaged from 0 to 40 fs) for a pump pulse intensity of 3×10^{14} W/cm^2. Grey shaded areas represent the uncertainty ranges of the curves. The black curve is a literature spectrum of bare Se^+ ions,[42] shifted by −0.08 eV. The color-coded lines on top of the spectrum and the transparent rectangles mark the energy intervals used to generate the time-traces shown in Figures 5 and 6.

may be readily identified with the depletion of parent neutral molecules by comparison with the static XUV absorption spectrum of selenophene in Figure 1. Features A, B, and C are tentatively assigned to emerging molecular species due to their immediate appearance at zero pump-probe delay and their relatively broad structure. A more concrete assignment, however, requires a more detailed analysis as outlined below.

C. Power dependence measurements

The red, green, and blue curves in Figure 4 represent spectra recorded at a delay of 2 ps using NIR intensities of 0.7, 1, and 3×10^{14} W/cm^2, respectively. The spectra have been scaled to the same parent molecule depletion signal at 57 eV and aligned vertically for easier comparison. The most prominent spectral change with increasing NIR intensity is the emergence of the sharp features in the 52-55 eV energy range, which are associated with Se^+ fragments. Furthermore, peak

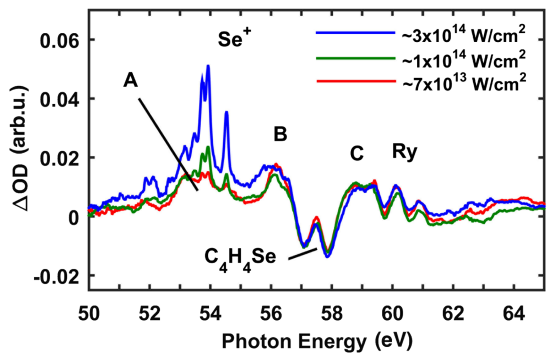

FIG. 4. Pump intensity dependence of XUV absorption spectra at 2 ps time delay. The spectra have been scaled to the same neutral molecule depletion around 57 eV and aligned vertically. The yield of Se^+ ions increases strongly with increasing NIR intensity, while the rest of the spectrum varies much less.

B develops a notable, additional low-energy component in the highest intensity spectrum.

D. Dynamics of spectral features

Figure 5 shows the time-dependent yields $I(t)$ of neutral selenophene (blue), Se^+ ions (black), and molecular species associated with feature A (yellow). The time traces have been obtained by integrating the data shown in Figure 2 over energy intervals of 57.0-57.5 eV (blue), 54.42-54.5 eV (black), and 54.30-54.35 eV (yellow), respectively, and subtracting contributions due to SFI-induced changes of the non-resonant continuum and valence absorption. These changes are noticeable as a shift of the entire spectrum to negative ΔOD in Figure 3 and effectively add a sloped, time-dependent background to the resonant spectral features. The background signal is approximated by a linear function spanning the entire energy range of the spectra and subtracted at each time step before deriving the time-dependent trends shown in Figures 5 and 6.

The green, red, and purple traces in Figure 6 illustrate the dynamics of feature C as well as the high and low energy shoulders of feature B, respectively, which were integrated over the energy ranges 58.8-59.1 eV (green), 56.3-56.45 eV (red), and 55.5-55.85 eV (purple). Note that the photon energy intervals chosen to derive the time traces in Figures 5 and 6 are indicated in Figure 3 by horizontal lines and transparent rectangles using the same color codes across all figures.

Note that, in particular, the Se^+ ion signal (Figure 5) does not rise before time zero, as would be expected for an instantly appearing or exponentially rising signal when taking the IRF into account. Instead, the signal starts becoming visible with respect to the noise only ~40 fs after zero pump-probe delay, which is marked by the vertical dashed line. The large gap between the two Se^+ ion lines around 54 eV, marked by an asterisk in Figures 2 and 3, provides access to the dynamics

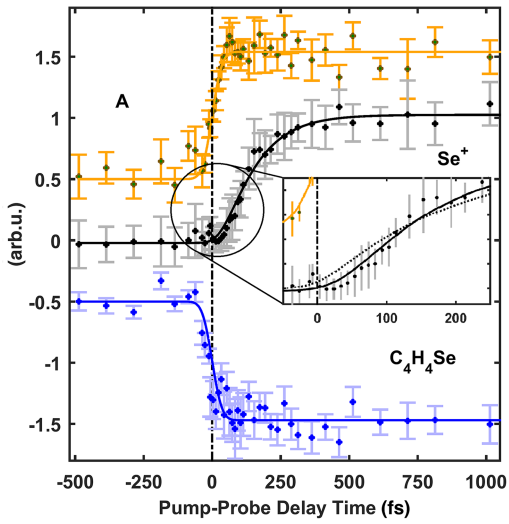

FIG. 5. Normalized pump-probe delay scans of the neutral selenophene depletion (blue), the rise of Se^+ ions (black), and the appearance of the molecular feature A, which is associated with a HOMO-1 vacancy (yellow). The yellow and blue traces are vertically shifted by ±0.5 for improved clarity. The inset shows a magnified view of the Se^+ time trace at small pump-probe delays and compares it to two different fit models: a single exponential rise (dotted) and a sequential two-step rise (solid).

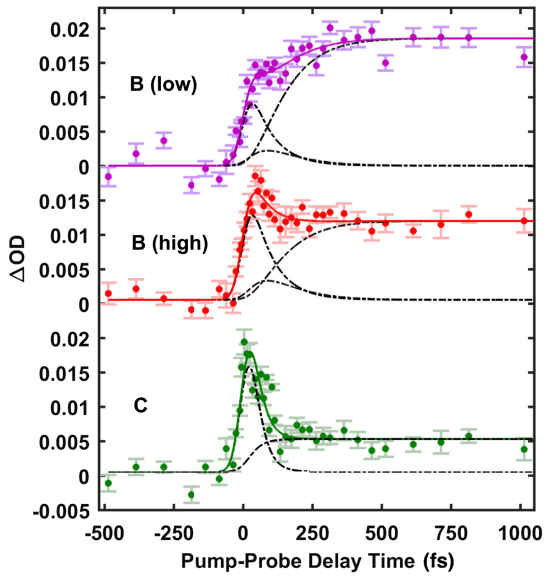

FIG. 6. Pump-probe delay scans of the molecular features B and C. The dynamics of feature B are separated into those of the low (purple) and the high (red) energy section of peak B. The green trace corresponds to the rapidly decaying feature C. Both fits for feature B shown in the upper two traces employ the same decay and rise time constants. The different fit components are indicated by dashed lines for each trace.

of feature A. This feature, which is underlying the Se^+ signal, has been taken into account in the derivation of the Se^+ trend shown in Figure 5. The intensity of feature A underneath the Se^+ peak has been estimated by its intensity just adjacent to the Se^+ peak and its shape recorded near zero delay, where contributions from Se^+ are negligible (Figure 3). The shape defines the ratio by which the adjacent A feature intensity is scaled before subtracting it from the Se^+ intensity. Note that this background subtraction procedure leads to a reduced scatter of the black Se^+ data points in Figure 5 that is smaller than expected from the statistically derived error bars, which are dominated by intensity variations of the high-order harmonic light.

V. ANALYSIS AND SPECTRAL ASSIGNMENTS

A. Modelling of the time traces

The blue trace in Figure 5 shows the expected trend of a signal associated with neutral parent molecules. The signal decreases within the experimental resolution as soon as the pump- and probe-pulses overlap and remains constant over the entire pump-probe delay range. The dynamics of feature A (yellow) mirror the parent molecule depletion. Feature A rises within the experimental time resolution and remains constant over the range of the experiment. Both signals are well described by step functions ($\theta(t)$) convoluted with a 67 fs wide Gaussian, which defines the IRF (solid lines in Figure 5). The two curves only differ in the sign of the signal change at zero delay.

The appearance of the Se^+ signal (black) is much more complex than that of feature A. Despite the 67 fs IRF, the Se^+ signal does not rise notably before ~40 fs pump-probe delay, a behavior that is typical for multi-step dynamics and that cannot be described by a direct dissociation. In order to describe the observed dynamic trend, we apply a two-step model that contains two characteristic time scales,

$$C_4H_4Se^{+*}\,(config.1) \xrightarrow{\tau_1} C_4H_4Se^{+*}\,(config.2) \xrightarrow{\tau_2} C_4H_4 + Se^+. \tag{1}$$

Within this model, the strong-field pulse prepares an excited cation (configuration 1) that decays with a rate $1/\tau_1$ to form an intermediate molecular species (configuration 2), which then dissociates to produce Se^+ ions with a rate $1/\tau_2$. In the following, this model will be tested against the observed experimental trends while the results of the *ab initio* calculations will be used to explore the electronic and structural characteristics of configurations 1 and 2. The final product yield $I(t)$ of a process as outlined in Equation (1) is described by a bi-exponential model function,

$$I(t) = a_2\left(1 + \left[\frac{\tau_1\tau_2}{\tau_1-\tau_2}\left(\frac{1}{\tau_1}e^{-\frac{t}{\tau_2}} - \frac{1}{\tau_2}e^{-\frac{t}{\tau_1}}\right)\right]\right)\theta(t) * IRF. \tag{2}$$

This function is used to describe the Se^+ trend in Figure 5 (black curve) using a nonlinear least squares fit procedure. Leaving both time constants freely floating leads to $\tau_1 \approx \tau_2 \approx 80 \pm 30$ fs. Since Equation (2) is not applicable for $\tau_1 = \tau_2$, the fit result has been confirmed by using the following equation, which describes a two-step process whereby the population and decay of the intermediate state proceed with equal rates:

$$I(t) = a_3\left(1 - \left(\frac{t}{\tau_{1,2}} + 1\right)e^{-\frac{t}{\tau_{1,2}}}\right)\theta(t) * IRF. \tag{3}$$

As can be seen by the solid black curve in Figure 5, the model yields a reasonable fit result. In contrast, restricting the fit to only a single exponential rise (i.e., a direct dissociation of configuration 1 with no intermediate configuration 2) leads to an average rise time of $\tau_1 \approx 200$ fs and does not give a satisfactory description of the Se^+ signal dynamics. The corresponding fit result is indicated by the dotted line in the inset of Figure 5.

The analysis of the time-dependent Se^+ yield suggests that the elimination of Se^+ ions involves (at least) a two-step relaxation mechanism that connects the initial molecular excitation with the final double-bond break. Based on the fit results described above, we conclude that the overall process takes approximately 170 fs to be completed (defined as the time it takes to form a fraction of 1−1/e of the product Se^+ ions) and proceeds with the involvement of two dynamic timescales of $\tau_1 \approx \tau_2 = 80 \pm 30$ fs.

Turning to molecular features B and C, the traces in Figure 6 indicate that both rise within the IRF of the experiment and exhibit signatures of at least two dynamic components, one of which is significantly longer-lived than the range of the experiment. In particular, peak C (green) and the high energy side of peak B (red) also show clear indications for a fast decaying channel.

As evident from Figures 2, 3, and 6, the low and high energy shoulders of peak B exhibit significantly different dynamic trends. To consistently model the entire feature, we assume that the traces extracted from both sides of the peak are composed of the same underlying dynamic contributions, and only the relative amplitudes of these contributions differ

for the low and high energy curves. Furthermore, we test the hypothesis that the individual contributions may be connected by the same dynamics concept as outlined in Equation (1) by employing the same time constants $\tau_1 \approx \tau_2 = 80$ fs as derived above. This approach leads to the following model function:

$$I(t) = \left[a_4 e^{-\frac{t}{\tau}} + \frac{b_4 t}{\tau} e^{-\frac{t}{\tau}} + c_4 \left(1 - \left(\frac{t}{\tau} + 1\right) e^{-\frac{t}{\tau}}\right)\right] \theta(t) * IRF, \tag{4}$$

where $\tau = 80$ fs is a fixed time constant and the amplitudes a_4, b_4, and c_4 represent the relative contributions of the initially prepared cation, the transient molecular species, and the final products, respectively. Varying only a_4, b_4, and c_4 during the fit procedure while keeping τ fixed results in the solid purple and red curves shown in Figure 6. Both curves provide an excellent description of the data despite the stark differences between the low and high energy trends. The individual dynamic contributions are indicated by dashed black lines.

The dynamics of feature C (green trace in Figure 6) are modeled using the following equation comprising an exponential decay and a single exponential rise:

$$I(t) = \left[a_5 e^{-\frac{t}{\tau_1}} + b_5 \left(1 - e^{-\frac{t}{\tau_2}}\right)\right] \theta(t) * IRF. \tag{5}$$

The corresponding fit gives a very good description of the data (solid green line) and indicates decay and rise times of $\tau_1 = 35^{+20}_{-10}$ fs and $\tau_2 = 30^{+90}_{-15}$ fs, respectively. Both time constants are shorter than the instrument response, although the uncertainty of τ_2 is quite significant. Note that the amplitude of the long-lived component of feature C is relatively small compared to the background correction of continuum absorption features described above (also see Figure 3). Therefore, residuals of an imperfect correction may notably contribute to this signal and we refrain from any further physical interpretation of this specific component.

The analysis suggests that the appearance of the atomic Se^+ fragments as well as the signals underlying feature B may be described by a two-step model as outlined in Equation (1). However, since peak B lies outside the spectral range of Se^+ ions, the nature of the final products represented by amplitude c_4 is still to be determined. We note that the intermediate state contribution to the dynamic trends of feature B is rather weak and similarly good fit results may be achieved when suppressing it completely while adjusting amplitudes a_4 and c_4 correspondingly or by representing the combination of the intermediate and final states by a single exponential rise with a time constant on the order of ~160 fs. Therefore, the chosen model function is by no means uniquely well suited to describe the experimental data. The important finding, however, is that the same dynamic concept used to describe the appearance of the Se^+ fragments *can* be used to achieve a very good description of the complex dynamics underlying feature B. Applying the empirical principle that the most likely physical explanation of the experimental observations is one that employs the least amount of independent parameters to consistently describe all observed trends, we propose that the dynamic trends underlying feature B and the appearance of the Se^+ fragments are closely related with the caveat that the final products within feature B are not Se^+ ions and their nature needs to be investigated with the aid of *ab initio* calculations as outlined below.

The instant rise and very fast decay of feature C may lead to speculations that it represents an initially prepared state whose decay may feed intensity into feature B. This possibility has been tested by performing fits in which peak B is comprised only of intermediate and final state contributions using time constants of both 35 fs and 80 fs. The corresponding fit results (not shown), however, give very poor representations of the data owing to the instant rise of feature B within the experimental IRF.

We note that we have also tried to perform a global fit analysis in which the temporal evolution of the entire spectrum is approximated by a two-dimensional fit function $f(E, t)$. However, the multitude of time scales and overlapping dynamic channels entailed in the recorded data results either in a poor global fit quality or in an ill-defined fit result depending on the number of free fit parameters. We have therefore decided to proceed as described above, employing multiple local fits for different features, which provides better control over the search space and the adequate number of free fit parameters for each region of interest.

B. Theoretical description and simulated XUV absorption spectra

Our calculations encompass a variety of XUV absorption spectra for the ground and excited states of C_4H_4Se and $C_4H_4Se^+$ within ~5 eV of the respective ground states, as well as the $C_4H_4Se^{++}$ ground state. Even though the DFT results represent spectra for fully relaxed geometries, some electronic states exhibit characteristic features that can be used to fingerprint the observed spectral structures that are stable on the 2 ps time scale of the experiment and, to a lesser extent, transient components; see supplementary material for details. Absorption spectra for 29 different configurations, labeled C1 to C29, can be found in the supplementary material. Figure 7 shows four examples of simulated differential absorption spectra that are most relevant for the following discussion. The simulations are compared to the measured Se 3d inner-shell absorption spectra near time zero (dark blue) and beyond 280 fs (red). In particular, Figure 7 shows the differential XUV absorption spectra of the cation ground state $\tilde{X}$ (black, C11—cyclic), the first excited cationic state $\tilde{A}$ (light blue, C12—cyclic), the HOMO → σ* excited cation (orange, C16—ring-open), and the $C_4H_4Se^{++}$ ground state (green, C26—cyclic). Note that in this notation, the HOMO → σ* excitation refers to the HOMO and σ* orbitals in the cyclic molecular cation ground state, which are not identical to the corresponding orbitals in the neutral molecule. Details about the labeling can be found in the supplementary material.

While the 4 simulated showcase spectra in Figure 7 comprise only a small fraction of the 29 spectra derived in the supplementary material, they are a good representation of physically relevant configurations based on a procedure of exclusion. For example, many of the principally possible excited states discussed in the supplementary material can be ruled out because they would exhibit strong absorption features below 53 eV, which are not observed in the experiment.

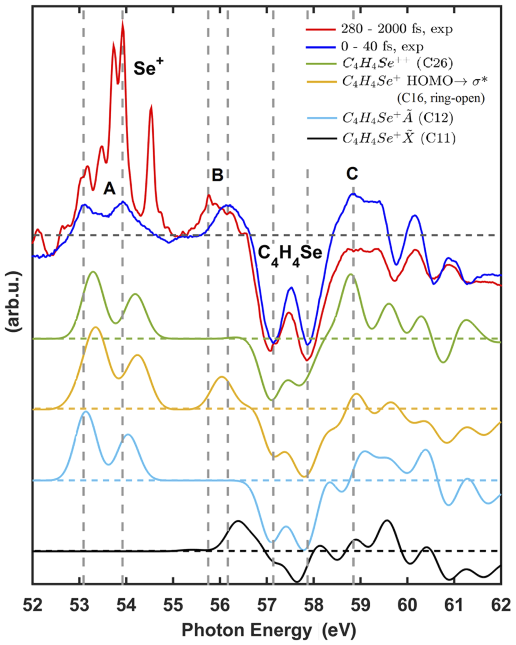

FIG. 7. Experimental time zero (dark blue) and long-time (red) spectra compared to selected calculated differential XUV absorption spectra. Shown are the spectra of the cation ground state $\tilde{X}$ (black), the first excited state $\tilde{A}$ (light blue), the non-cyclic σ* excited cation (orange), and the $C_4H_4Se^{++}$ ground state.

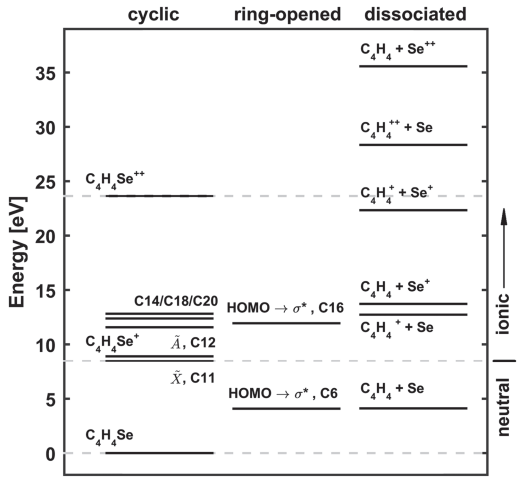

FIG. 8. Calculated energies of several cationic and dicationic states with cyclic (left) and ring-opened (middle) geometries, relative to the selenophene ground state energy. Right: Appearance energies for several dissociation channels. Dashed lines mark the ground state energies of the neutral molecule, the cation, and the dication. Labels C6, C11, etc., refer to molecular configurations described in the text and the supplementary material.

This leads to the conclusion that only electrons from the HOMO and HOMO-1 orbitals of the neutral molecule are subject to strong-field excitation and/or ionization in this experiment at the employed field intensities. Furthermore, only spectra of species that give rise to a clean depletion signal around 57.5 eV, as observed in the experiment, can contribute in a notable amount to the overall spectrum.

An important finding from the calculation is that an excitation into the σ* orbital (orbital number 33 in the supplementary material section) leads to a breaking of the C–Se bond and an opening of the selenophene ring. In contrast, π* excitations lead to a buckling of the ring but not to an opening.

Figure 8 shows the energies of several cationic and dicationic states in cyclic (left) and ring-opened (middle) geometries, relative to the selenophene ground state. Energies required for the production of various dissociation products are shown on the right. The energy levels are drawn from the same calculations used to simulate the XUV spectra, see supplementary material.

The relatively high threshold for the production of Se^+ ions compared to many molecular species is consistent with the finding that Se^+ ions are only observed for higher pump pulse intensities while molecular species (features A, B) are always observed (Figure 4). However, the fact that we observe bare Se^+ ions in both high-intensity ($\geq 10^{14}$ W/cm^2) long delay spectra (Figure 4) suggests that the employed field intensities are beyond the regime where a substantial amount of excited neutrals are produced, since the elimination of Se^+ requires the population of highly (~5.2 eV) excited cation states. This conclusion is also supported by the absence of a clear spectral signature of bare Se atoms in the experiment, which would be produced upon excitation of dissociative excited states in the neutral molecule. Furthermore, the dominance of Se^+ ions compared to Se neutrals in both high-intensity measurements indicates that the $C_4H_4 + Se^+$ dissociation channel of molecular cations is favored over the energetically lower lying $C_4H_4^+ + Se$ asymptote. The physical origin for this selectivity is not known.

C. Parent molecule depletion

The depletion signals, which are marked as deep blue zones in Figure 2 and negative ΔOD values in Figure 3, appear instantly as soon as pump and probe pulses overlap and the features remain essentially constant throughout the entire range of time delays. These dynamics suggest that the signals are associated with the depletion of parent ground state molecules. The assignment is strongly supported by the double peak structure in the 57-58 eV range that mirrors the static absorption peaks a, b of the parent molecule in Figure 1(a) as well as the broad structures below ~53 eV and above ~61 eV that are reminiscent of the valence ionization contributions in Figure 1(a). We therefore assign all regions with significant negative ΔOD values to a depletion of ground state selenophene molecules by strong-field-induced excitation and/or ionization. Note that changes in the Rydberg features (Ry) near 60 eV already appear around −250 fs. This effect is attributed to a weak NIR pre-pulse that induces transient absorption and transmission effects before the main peak arrives at the target. The sensitivity of XUV transitions involving Rydberg states to relatively modest NIR field strengths has previously been demonstrated in experiments on atomic Xe and its appearance in Figure 2 gives further support to the spectral assignments near 60 eV.[27]

D. Species associated with feature A

Feature A appears instantly and remains constant on the time scale of the experiment. It is, therefore, most likely associated with one or more molecular species that are populated by the interaction of the parent molecule with the pump laser and that remain stable for at least several picoseconds.

The theoretical results clearly favor the assignment of this feature to transitions from Se 3d orbitals to vacancies in the HOMO-1 orbital of the parent neutral molecule (see double peak structures for cyclic cations around 53.5 eV in Figure 7). Note that this assignment is not equivalent to an identification of the feature with the first excited $\tilde{A}$ cationic state, since various other excited states also exhibit HOMO-1 vacancies. The correlation between the double-peak feature near 53.5 eV and a HOMO-1 vacancy is also reproduced by an alternative, more qualitative approach to spectral assignments that employs a Koopmans' picture in combination with orbital overlap arguments. Within this approach, the peak positions corresponding to transitions from core orbitals to valence vacancies are estimated by the difference between core- and valence-electron binding energies.[19] The binding energies of selenophene Se $3d_{3/2}$, Se $3d_{5/2}$, HOMO-1, and HOMO electrons are 62.1 eV, 61.1 eV, 9.12 eV, and 9.00 eV, respectively.[40,43] These energies would suggest a double peak structure with energies of ~52 eV (= 61.1 eV – 9.1 eV) and ~53 eV (= 62.1 eV – 9.1 eV) for transitions from the $3d_{5/2}$ and $3d_{3/2}$ levels, respectively, into a HOMO-1 vacancy, which approximately matches the structure of feature A. Note, though, that the HOMO and HOMO-1 orbitals are almost degenerate, which makes a spectral assignment based on peak positions alone challenging. However, the electron density of the neutral parent molecule HOMO orbital at the Se atom is vanishingly small while the HOMO-1 orbital is dominated by contributions from Se valence electrons.[5] Hence, within the Franck-Condon approximation, only transitions from the Se 3d orbitals into HOMO-1 orbital vacancies are expected to have significant oscillator strengths. This qualitative picture is supported by the calculated cation $\tilde{X}$ and $\tilde{A}$ differential absorption spectra in Figure 7, where the first corresponds to a HOMO ionized configuration and the latter to a HOMO-1 vacancy. Hence, we assign feature A to excited molecular ions that are associated with a vacancy in the HOMO-1 orbital of the neutral molecule. This assignment includes, in particular, the cationic $\tilde{A}$ state.

E. Species associated with feature B

Peak B is the most pronounced spectral feature at the lowest excitation energy, while no sharp atomic features are observed (7×10^{13} W/cm^2, Figure 4). Based on the energy ordering displayed in Figure 8 and the pronounced peak of the simulated cation ground state XUV spectrum near 56 eV (black trace in Figure 7), it is tempting to interpret the low NIR intensity spectrum predominantly as the signature of stable (on the ps time scale of the experiment) cyclic cations in the $\tilde{X}$ ground and $\tilde{A}$ lowest excited states. Indeed, as becomes evident from Figure 9, the spectrum can be reasonably well simulated by a linear combination of the (differential) calculated $\tilde{X}$ and $\tilde{A}$ cation absorption spectra with an intensity ratio of 2:3. The agreement between theory and experiment is within the accuracy of the calculation. The 2:3 ratio appears reasonable since the HOMO and HOMO-1 orbitals are almost degenerate and one may speculate that electrons from both orbitals are subject to ionization by the strong field with similar cross sections. The simulation reproduces, in particular, feature B very well, which originates

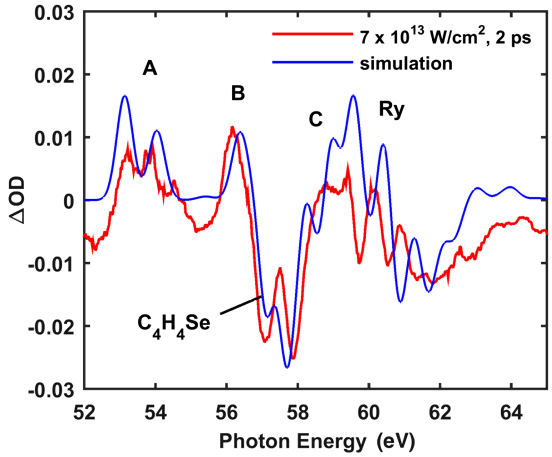

FIG. 9. Experimental low intensity spectrum (red) recorded at 7×10^{13} W/cm^2 compared to a calculated differential XUV absorption spectrum (blue) composed of a 2:3 ratio of the $\tilde{X}$ and $\tilde{A}$ state spectra of $C_4H_4Se^+$, which correspond to a HOMO and a HOMO-1 vacancy, respectively.

in this picture from ground state cations (see Figure 7), while the HOMO-1 vacancy features of the $\tilde{A}$ state cations are responsible for feature A. The good agreement between simulation and experiment suggests that, at the lowest field intensity, cations are predominantly generated in the two lowest lying electronic states with feature A emerging from the $\tilde{A}$ state and feature B from the $\tilde{X}$ state. We note that signal contributions from highly excited neutral Rydberg states cannot be excluded as they may exhibit similar absorption features as the two lowest cation states.

At higher field intensities (3×10^{14} W/cm^2) and long time delays, however, feature B extends further to lower energies (Figures 3 and 4) and comprises a decaying and a rising component with their relative intensities dependent on the chosen energy interval (Figure 6). While the low energy part is dominated by the rising component, the high-energy part exhibits a more pronounced decaying contribution. Intriguingly, the only calculated cation spectrum that gives rise to an intense absorption signal at the low energy side of peak B without significant absorption below 53 eV is the one associated with the HOMO → σ* excited cation configuration. As our calculations show, this configuration corresponds to a ring-opened structure, see middle column in Figure 8. Therefore, the rising contribution underlying peak B is interpreted as the spectral signature of a ring opening and subsequent relaxation after cleavage of one of the Se–C bonds. The assignment to a ring-opening process is supported by the fact that the low energy part of feature B becomes particularly prominent at the highest NIR intensity, which enables the population of higher lying cation states such as the cationic HOMO → σ* configuration. As described in Sec. V A, the entire process of reaching the open ring structure may be modeled by the same two-step mechanism that leads to the production of Se^+ ions. We, therefore, propose that both the relaxed open-ring HOMO → σ* configurations and the Se^+ fragments are the result of very similar relaxation dynamics that proceed on the same electronic surfaces but may either lead to a single bond break to form a stable, non-cyclic molecule or to a double bond break to release Se^+ ions, depending on the amount of vibrational excitation in the σ* excited state.

In contrast to the low energy part of feature B, which is assigned to ring-opening dynamics, the high energy part may also contain a prompt, long-lived contribution originating from the instantly populated cation ground state (Figure 9) or a buckled excited state configuration (e.g., C18 or C20). Note that this is not considered by the employed fit model that uses the time constants obtained from the Se^+ trace. However, a prompt contribution will effectively only add a constant offset and will thus only affect the amplitudes of the individual contributions and not the time constants.

F. Species associated with feature C

An assignment of feature C around 59 eV is difficult because all cationic states absorb in the respective energy regime. Interestingly, the $C_4H_4Se^{++}$ ground state (Figure 7, green spectrum) exhibits a particularly strong maximum at the position of feature C. As the present study is carried out in the low 10^{14} W/cm^2 regime, only the production of singly ionized parent molecules and some fragmentation are expected,[44–47] but no significant double ionization or Coulomb explosion.[48–52] Significant double ionization for this class of molecules is typically only observed beyond 5×10^{14} W/cm^2.[51] For furan, for example, the double ionization threshold has been determined to 8×10^{14} W/cm^2.[51]

Yet, the spectra of highly excited cation Rydberg states (beyond the scope of our calculation) will also resemble the $C_4H_4Se^{++}$ ground state absorption spectrum. Hence, for high pump laser intensities, we favor the assignment of feature C to rapidly decaying highly excited $C_4H_4Se^+$ ions. Since the experimental method is not sensitive to charge states, we cannot completely rule out the generation of doubly charged cations. Power dependent mass spectrometry experiments of strong field ionized selenophene could help to better evaluate the role of $C_4H_4Se^{++}$ at the employed NIR intensities. Note that if dications would be produced, they may also act as a source of bare Se^+ ions, given that even the dication ground state is energetically unstable relative to the $C_4H_4^+ + Se^+$ dissociation channel.

VI. DISCUSSION

With the assignments and analysis from Secs. IV and V at hand we can now proceed to develop a more general picture of the SFI induced dynamics in selenophene. The proposed reaction pathways are sketched in Figure 10.

At the lowest field intensities ($<10^{14}$ W/cm^2), experiment and theory can be directly compared (Figure 9) and all spectral features are reproduced reasonably well by a combination of the ground ($\tilde{X}$) and first excited ($\tilde{A}$) state spectra of the parent molecular cation (corresponding to HOMO and HOMO-1 vacancies, respectively). Therefore, we conclude that, in this intensity regime, mainly stable cyclic molecular ions (on the 2 ps time scale of the experiment) in the lowest two electronic states are produced.

At higher field intensities ($>10^{14}$ W/cm^2), higher excited states are accessed, thereby initiating ring-opening and dissociation dynamics as sketched in Figure 10. Two different spectral features give insight into the ring-opening dynamics in the selenophene cation: the Se^+ fragment yield and the dynamic

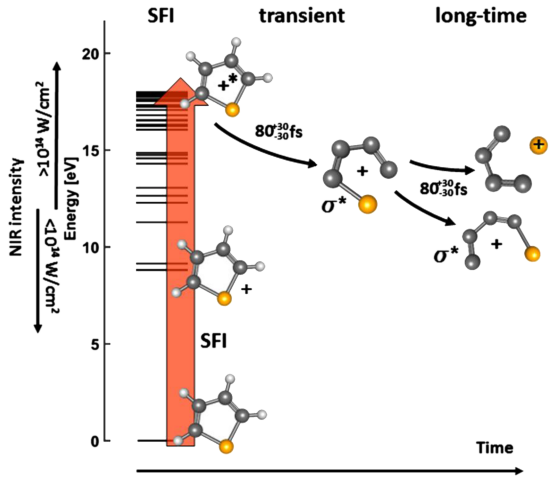

FIG. 10. Schematic representation of the proposed ring-opening and dissociation pathways and associated time scales. The initial strong-field ionization (SFI) phase is characterized by an IRF of 67 fs. Below ~10^{14} W/cm^2 stable cyclic selenophene cations in the electronic ground and first excited state are the predominant products. Above this pump pulse intensity, ring-opening and fragmentation dynamics are induced that most likely proceed with the involvement of σ* excited cation states.

trends underlying feature B. The dynamics of both spectroscopic features may be described within the same two-step model, whereby an initially excited cation state relaxes into an intermediate molecular configuration within (80 ± 30) fs and eventually leads to either stable cations in σ* excited states or to dissociation to produce Se^+ fragments within an additional (80 ± 30) fs. This interpretation is based on the fact that only σ* excited cation states are expected to exhibit prominent features in the range of the low energy shoulder of peak B and, according to our calculations, all these configurations lead to an opening of the ring. The assignment is supported by the intensity dependence of the feature, which agrees with the expectation that a ring opening requires additional energy deposition in the molecule compared to the cation ground state. We tentatively assign the first step to a transition from a highly excited cyclic cation to a σ* excited state in which one of the C–Se bonds is broken but the arrangement of nuclei is still close to the original molecule. The outcome of the second step may be defined by the amount of vibrational excitation in the σ* state. The σ* excited cation is thermodynamically stable with respect to the $C_4H_4 + Se^+$ dissociation in its vibrational ground state, but in vibrationally excited states (≥1.8 eV above the ground state) dissociation is possible (Figure 8). Thus, the observed dynamics may be associated with σ* excited cation states that are generated with different amounts of vibrational energy. Some of these intermediate configurations associated with the σ* potential energy surface (PES) relax to give stable ring-opened states as manifested in the temporal behavior of feature B. Beyond ~2 eV of stored vibrational energy, however, the intermediate configurations may become unstable and undergo dissociation to produce Se^+ ions.

It is noteworthy that the calculated vibrational period of the C–Se asymmetric stretch mode in selenophene is ~90 fs (see supplementary material). The excellent agreement of this value with the characteristic time scales for both steps in the observed ring-opening dynamics is most likely fortuitous. However, it is significant that we manage to observe distinct

steps within a complex ring-opening reaction that proceed on the time scale of a single vibrational period of the critical bond(s) involved in this reaction. This observation indicates an extremely efficient coupling between electronic and nuclear degrees of freedom inside the molecule that must be driving the photo-induced ring-opening.

Note that we cannot exclude the participation of higher excited states beyond the scope of our calculations and with similar absorption features as the σ* excited configurations as well as a coincidental agreement between the time scales found for different spectral features. Therefore, stable non-cyclic cations may be produced on a ~170 fs time scale independently from the dynamics outlined above. Furthermore, other contributions such as, for example, from a buckled excited state (e.g., C18 or C20, see the supplementary material) that may decay further to lower states, are also consistent with the spectral position of peak B and proposing a unique assignment is challenging.

The rapidly (35^{+20}_{-10} fs) decaying feature C is attributed to highly excited cation Rydberg states (even though we cannot fully rule out that $C_4H_4Se^{++}$ contributes to this feature). The signal decays faster than the IRF and reflects dynamics during the initial phase of the strong-field induced processes, similar to the instantly rising and fast decaying component of feature B. Note that based on the detailed analysis of the time traces we exclude the possibility that peak C is an initially prepared state whose decay gives rise to the emergence of the instantly rising part of feature B. However, it is possible that the decay of feature C leads to intermediate and/or final states with spectral signatures within the range of feature B for delays beyond a few 10 fs. Future studies with more precisely controlled excitation schemes employing UV pump pulses may enable a better differentiation of the relaxation pathways observed herein.

It is instructive to compare our results to those for ring-opening dynamics in other (neutral) heteronuclear five-membered ring molecules. Among these molecules, most effort has been spent on the investigation of the photo-induced dynamics in thiophene.[10–12] The exact relaxation pathways, however, are not well understood and are subject to ongoing discussions. It has been reported that UV excitation (~240 nm) of thiophene initiates vibrational dynamics in an excited state (80 fs), followed by an ultrafast decay via a conical intersection, presumably a ring-opening (25 fs). A theoretical study on the ultrafast photo-induced dynamics of furan[9] has been reported, suggesting similar dynamics for this molecule. The ring-opening dynamics observed for the selenophene cation proceed with the participation of two steps, each of which is marked by an ~80 fs relaxation time scale. This result is very reminiscent of the time scales observed for the ultra-fast dynamics in thiophene.

Another example of a well-studied ultra-fast ring opening processes in a cyclic, organic molecule is the photo-induced ring-opening in 1,3-cyclohexadiene.[3,52–55] In this molecule, UV excitation leads to the population of a very rapidly decaying state (~35 fs). Subsequently, upon passage through two conical intersections, the entire photochemical ring-opening reaction proceeds within about 140 fs during which 5 eV of electronic energy are converted into vibrational motion of nuclei[3] and the molecule eventually reaches the ring opened 1,3,5-hexatriene ground state.

Due to the complex nature of the SFI process, many different initially excited states can simultaneously contribute to the observed dynamics presented here. Hence, it is much more difficult to interpret the observed dynamics than it is for the UV-induced ring-opening reactions. However, it is intriguing that we observe similar time-scales. Even though the above examples refer to neutral molecules, the time-scales for ring-opening reactions may essentially be determined by the time it takes the molecule to pass through intersection on its way to the ring opened products. The fact that the time scales associated with the ring-opening process are on the order of a single vibrational period along the critical bond indicates that extremely efficient electronic-nuclear dynamics coupling is driving this reaction pathway in strong-field ionized selenophene, presumably also with participation by one or more conical intersections. Future transient XUV absorption studies using UV excitation to initiate ring-opening dynamics will give access to well-defined, single-photon induced dynamic pathways. On the theory side, a detailed description of possible potential energy surfaces and their dynamic coupling should be obtained to complement the experimental and theoretical tools presented here. The combination of the existing capabilities with better defined dynamic pathways, higher temporal resolution, and more advanced theoretical guidance on possible reaction channels will give exclusive access to details of photo-induced ring-opening reactions from the exquisite perspective of a local reporter atom.

VII. CONCLUSION

Molecular dynamics initiated by strong-field ionization of selenophene molecules have been explored using femtosecond XUV transient absorption spectroscopy. The element specific nature of the method provides insight into the ring-opening and dissociation processes launched upon ionization from the distinct viewpoint of the Se atom.

Ionization of selenophene molecules with field intensities below 10^{14} W/cm^2 leads predominantly to the formation of stable cations in their two lowest lying electronic states, corresponding to HOMO and HOMO-1 vacancy configurations. The low intensity spectrum is well reproduced by a simulation using just these two configurations.

At intensities of $\sim 3 \times 10^{14}$ W/cm^2, strong-field ionization leads to various products such as stable open ring cations as well as fragmented molecules where both C–Se bonds have been broken. The fingerprint of the spectral feature associated with the ring-open structure is consistent with the calculated spectrum for a σ* excited cation configuration that leads to an open ring geometry. The emergence of both the stable ring-open configuration as well as the Se^+ ions can be described within the same two-step model involving two time scales of $\tau_1 \approx \tau_2 = 80 \pm 30$ fs. We tentatively assign the first step to a relaxation of a highly excited cyclic cation state to a σ* excited state with only one C–Se bond but a nuclear configuration similar to the original molecule. The second step proceeds on the σ* PES and leads either to a stable ring-open configurations or, beyond ~2 eV of stored vibrational energy, to the scission of the

remaining C–Se bond. Interestingly, the observed time-scales for the ring opening reactions are similar to the time-scales reported for ring opening reactions in neutral thiophene[10–12] and 1,3-cyclohexadiene[3,52–55] and the observed reaction steps proceed within the time scale of a single vibrational period along the critical C–Se bonds. This indicates that extremely efficient coupling between electronic and nuclear degrees of freedom is driving the ring-opening mechanisms, presumably with the involvement of one or several conical intersections, as has been pointed out in previous studies on other molecules.

The present work demonstrates the ability of transient XUV absorption spectroscopy to explore transition states in complex ultrafast dynamics from a local perspective. Future experiments will be geared toward the study of single UV-photon-induced ring-opening dynamics of aromatic molecules, enabling a better defined population of specific excited states. As the present work suggests, relaxation dynamics in neutral selenophene may be studied at the Se 3d edge and it will be interesting to compare the ultrafast UV-induced ring-opening dynamics to those in the strong-field ionized species.

The rapid development of HHG based XUV and soft-X-ray light sources will facilitate the exploration of molecular dynamics at even higher photon energies and may provide access to the sulfur 2p or carbon 1s edges in the near future, enabling the study of ring-opening dynamics in a variety of interesting molecules, such as thiophene, furan and other cyclic organic molecules.

SUPPLEMENTARY MATERIAL

See supplementary material for a detailed description of the theoretical calculations.

ACKNOWLEDGMENTS

This work was supported by the U.S. Department of Energy, Office of Basic Energy Sciences, Chemical Sciences, Geosciences and Biosciences Division, through Contract No. DE-AC02-05CH11231. F.L. would like to acknowledge support by the Austrian Science Fund (FWF, Erwin Schrödinger Fellowship Grant No. J 3580-N20). Theoretical simulations were performed on the Cray XE6 Hopper computer at the National Energy Research Scientific Computing Center (NERSC-LBNL) and Molecular Foundry computing resources, Nano and Vulcan, managed by the High Performance Computing Services Group of LBNL.

[1] C. M. Beaudry, J. P. Malerich, and D. Trauner, Chem. Rev. **105**, 4757–4778 (2005).
[2] R. B. Woodward and R. Hoffmann, Angew. Chem., Int. Ed. Engl. **8**, 781–853 (1969).
[3] S. Deb and P. M. Weber, Annu. Rev. Phys. Chem. **62**, 19–39 (2011).
[4] M. P. Minitti, J. M. Budarz, A. Kirrander, J. S. Robinson, D. Ratner, T. J. Lane, D. Zhu, J. M. Glownia, M. Kozina, and H. T. Lemke, Phys. Rev. Lett. **114**, 255501 (2015).
[5] I. Powis, I. Zaytseva, A. Trofimov, J. Schirmer, D. Holland, A. Potts, and L. Karlsson, J. Phys. B: At., Mol. Opt. Phys. **40**, 2019 (2007).
[6] M. M. Campos-Vallette and R. E. Clavijo C, Spectrosc. Lett. **18**, 759–766 (1985).
[7] A. Trombetti and C. Zauli, J. Chem. Soc. A **1967**, 1106–1111.
[8] J. Pola and A. Ouchi, J. Org. Chem. **65**, 2759–2762 (2000).
[9] N. Gavrilov, S. Salzmann, and C. M. Marian, Chem. Phys. **349**, 269–277 (2008).
[10] R. Weinkauf, L. Lehr, E. Schlag, S. Salzmann, and C. Marian, Phys. Chem. Chem. Phys. **10**, 393–404 (2008).
[11] S. Salzmann, M. Kleinschmidt, J. Tatchen, R. Weinkauf, and C. M. Marian, Phys. Chem. Chem. Phys. **10**, 380–392 (2008).
[12] G. Cui and W. Fang, J. Phys. Chem. A **115**, 11544–11550 (2011).
[13] E. E. Rennie, D. M. P. Holland, D. A. Shaw, C. A. F. Johnson, and J. E. Parker, Chem. Phys. **306**, 295–308 (2004).
[14] K. Takimiya and T. Otsubo, Phosphorus, Sulfur Silicon Relat. Elem. **180**, 873–881 (2005).
[15] I. F. Perepichka and D. F. Perepichka, *Handbook of Thiophene-Based Materials: Applications in Organic Electronics and Photonics* (Wiley Online Library, 2009).
[16] R. J. Levis and M. J. DeWitt, J. Phys. Chem. A **103**, 6493–6507 (1999).
[17] M. Lezius, V. Blanchet, D. M. Rayner, D. M. Villeneuve, A. Stolow, and M. Y. Ivanov, Phys. Rev. Lett. **86**, 51 (2001).
[18] A. E. Boguslavskiy, J. Mikosch, A. Gijsbertsen, M. Spanner, S. Patchkovskii, N. Gador, M. J. Vrakking, and A. Stolow, Science **335**, 1336–1340 (2012).
[19] M.-F. Lin, D. M. Neumark, O. Gessner, and S. R. Leone, J. Chem. Phys. **140**, 064311 (2014).
[20] Z.-H. Loh and S. R. Leone, J. Chem. Phys. **128**, 204302 (2008).
[21] E. R. Hosler and S. R. Leone, Phys. Rev. A **88**, 023420 (2013).
[22] A. S. Chatterley, F. Lackner, D. M. Neumark, S. R. Leone, and O. Gessner, Phys. Chem. Chem. Phys. **18**, 14644–14653 (2016).
[23] E. Goulielmakis, Z.-H. Loh, A. Wirth, R. Santra, N. Rohringer, V. S. Yakovlev, S. Zherebtsov, T. Pfeifer, A. M. Azzeer, M. F. Kling, S. R. Leone, and F. Krausz, Nature **466**, 739–743 (2010).
[24] Z.-H. Loh, C. H. Greene, and S. R. Leone, Chem. Phys. **350**, 7–13 (2008).
[25] Z.-H. Loh, M. Khalil, R. E. Correa, R. Santra, C. Buth, and S. R. Leone, Phys. Rev. Lett. **98**, 143601 (2007).
[26] S. G. Sayres, E. R. Hosler, and S. R. Leone, J. Phys. Chem. A **118**, 8614–8624 (2014).
[27] M.-F. Lin, A. N. Pfeiffer, D. M. Neumark, S. R. Leone, and O. Gessner, J. Chem. Phys. **137**, 244305 (2012).
[28] A. R. Attar, L. Piticco, and S. R. Leone, J. Chem. Phys. **141**, 164308 (2014).
[29] A. R. Attar, A. Bhattacherjee, and S. R. Leone, J. Phys. Chem. Lett. **6**, 5072–5077 (2015).
[30] Z.-H. Loh and S. R. Leone, J. Phys. Chem. Lett. **4**, 292–302 (2013).
[31] A. C. Thompson, J. Kirz, D. T. Attwood, E. M. Gullikson, M. R. Howells, J. B. Kortright, Y. Liu, and A. L. Robinson, *X-Ray Data Booklet*, 3rd ed. (Lawrence Berkeley National Laboratory, Berkeley, CA, 2009).
[32] W. Kohn and L. J. Sham, Phys. Rev. **140**, A1133 (1965).
[33] P. Hohenberg and W. Kohn, Phys. Rev. **136**, B864 (1964).
[34] E. Runge and E. K. Gross, Phys. Rev. Lett. **52**, 997 (1984).
[35] A. T. Gilbert, N. A. Besley, and P. M. Gill, J. Phys. Chem. A **112**, 13164–13171 (2008).
[36] Y. Zhang, J. D. Biggs, D. Healion, N. Govind, and S. Mukamel, J. Chem. Phys. **137**, 194306 (2012).
[37] M. E. Casida, *Recent Advances in Density Functional Methods: Part I* (World Scientific, Singapore, 1995), Vol. 1, p. 155.
[38] T. M. Henderson, B. G. Janesko, and G. E. Scuseria, J. Chem. Phys. **128**, 194105 (2008).
[39] R. Baer, E. Livshits, and U. Salzner, Annu. Rev. Phys. Chem. **61**, 85–109 (2010).
[40] A. Hitchcock, G. Tourillon, and W. Braun, Can. J. Chem. **67**, 1819–1827 (1989).
[41] O. Shih, A. H. England, G. C. Dallinger, J. W. Smith, K. C. Duffey, R. C. Cohen, D. Prendergast, and R. J. Saykally, J. Chem. Phys. **139**, 035104 (2013).
[42] D. A. Esteves, R. C. Bilodeau, N. C. Sterling, R. A. Phaneuf, A. L. D. Kilcoyne, E. C. Red, and A. Aguilar, Phys. Rev. A **84**, 013406 (2011).
[43] I. Reineck, C. Nohre, P. Lodin, R. Maripuu, B. Lindberg, L. Karlsson, K. Siegbahn, A. B. Hornfeldt, and S. Gronowitz, Chem. Scr. **22**, 209–220 (1983).
[44] K. W. D. Ledingham, R. P. Singhal, D. J. Smith, T. McCanny, P. Graham, H. S. Kilic, W. X. Peng, S. L. Wang, A. J. Langley, and P. F. Taday, J. Phys. Chem. A **102**, 3002–3005 (1998).
[45] M. Castillejo, S. Couris, E. Koudoumas, and M. Martín, Chem. Phys. Lett. **308**, 373–380 (1999).
[46] A. N. Markevitch, D. A. Romanov, S. M. Smith, H. B. Schlegel, M. Y. Ivanov, and R. J. Levis, Phys. Rev. A **69**, 013401 (2004).

[47]A. D. Tasker, L. Robson, K. W. D. Ledingham, T. McCanny, S. M. Hankin, P. McKenna, C. Kosmidis, D. A. Jaroszynski, and D. R. Jones, J. Phys. Chem. A **106**, 4005–4013 (2002).
[48]P. Tzallas, C. Kosmidis, P. Graham, K. W. D. Ledingham, T. McCanny, S. M. Hankin, R. P. Singhal, P. F. Taday, and A. J. Langley, Chem. Phys. Lett. **332**, 236–242 (2000).
[49]S. Shimizu, J. Kou, S. Kawato, K. Shimizu, S. Sakabe, and N. Nakashima, Chem. Phys. Lett. **317**, 609–614 (2000).
[50]N. Nakashima, S. Shimizu, T. Yatsuhashi, S. Sakabe, and Y. Izawa, J. Photochem. Photobiol., C **1**, 131–143 (2000).
[51]C. Kosmidis, P. Tzallas, K. W. D. Ledingham, T. McCanny, R. P. Singhal, P. F. Taday, and A. J. Langley, J. Phys. Chem. A **103**, 6950–6955 (1999).
[52]S. A. Trushin, W. Fuss, T. Schikarski, W. E. Schmid, and K. L. Kompa, J. Chem. Phys. **106**, 9386–9389 (1997).
[53]N. Kuthirummal, F. M. Rudakov, C. L. Evans, and P. M. Weber, J. Chem. Phys. **125**, 133307 (2006).
[54]B. C. Arruda and R. J. Sension, Phys. Chem. Chem. Phys. **16**, 4439–4455 (2014).
[55]V. S. Petrović, M. Siano, J. L. White, N. Berrah, C. Bostedt, J. D. Bozek, D. Broege, M. Chalfin, R. N. Coffee, J. Cryan, L. Fang, J. P. Farrell, L. J. Frasinski, J. M. Glowania, M. Guehr, M. Hoener, D. M. P. Holland, J. Kim, J. P. Marangos, T. Martinez, B. K. McFarland, R. S. Minns, S. Miyabe, S. Schorb, R. J. Sension, L. S. Spector, R. Squibb, H. Tao, J. G. Underwood, and P. H. Bucksbaum, Phys. Rev. Lett. **108**, 253006 (2012).